Magnetic ground state of the dimer-based hexagonal perovskite Ba₃ZnRu₂O₉

S. Hayashida [1,*,†] H. Gretarsson [1,2] P. Puphal [1] M. Isobe [1] E. Goering [1] Y. Matsumoto [1]
J. Nuss [1] H. Takagi [1,3,4] M. Hepting [1,‡] and B. Keimer [1,§]

[1]*Max-Planck-Institute for Solid State Research*, Heisenbergstraße 1, 70569 Stuttgart, Germany
[2]*PETRA III, Deutsches Elektronen-Synchrotron DESY*, Notkestraße 85, 22607 Hamburg, Germany
[3]*Department of Physics, University of Tokyo*, Bunkyo-ku, Hongo 7-3-1, Tokyo 113-0033, Japan
[4]*Institute for Functional Matter and Quantum Technologies, University of Stuttgart*, 70550 Stuttgart, Germany

We investigate the magnetic ground state of single crystals of the ruthenium-dimer-based hexagonal perovskite Ba₃ZnRu₂O₉ using magnetic susceptibility and resonant inelastic x-ray scattering (RIXS) measurements. While a previous study on powder samples exhibited intriguing magnetic behavior, questions about whether the spin state within a Ru₂O₉ dimer is a conventional $S = 3/2$ dimer or an orbital-selective $S = 1$ dimer were raised. The RIXS spectra reveal magnetic excitations from Hund's intraionic multiplet and intradimer spin-triplet transitions. The observed transition energies of the Hund's intraionic multiplets align with the $S = 3/2$ ground state, contrasting with the theoretically proposed orbital-selective $S = 1$ dimer state. High-temperature magnetic susceptibility analysis confirms the realization of the spin $S = 3/2$ dimer state, and the extracted intradimer coupling is consistent with the spin-triplet transition energy observed in the RIXS spectra. These results highlights the ability of "spectroscopic fingerprinting" by RIXS to determine the magnetic ground states of complex materials.

I. INTRODUCTION

Hexagonal perovskites have served as an intriguing platform for quantum magnetism [1]. Unlike cubic perovskites, where metal-oxygen octahedra share corners, hexagonal perovskites are characterized by their face-sharing octahedral frameworks, which can result in the formation of dimers, trimers, tetramers, or even longer chains. The metal-metal distances in such networks are generally shorter (and the overlap of metal d-orbitals correspondingly larger) than those in networks of corner-sharing octahedra. This can lead to unusual magnetic quantum correlations [1,2].

Within this family, ruthenium-dimer-based hexagonal perovskites Ba₃MRu₂O₉ (M = cations), featuring Ru₂O₉ dimers, have been extensively studied. The oxidation state of M plays a crucial role in determining the valence state of the Ru atom, leading to a variety of magnetic states.

Magnetic cations such as Ni²⁺, Co²⁺, and rare-earth metal R^{3+} ions induce long-range magnetic order [3–12]. Notably, in systems with rare-earth metal ions, Ba₃RRu₂O₉ exhibits unusual magnetoelectric couplings [9,10,12]. On the other hand, nonmagnetic cations can also lead to diverse magnetic states in the Ru₂O₉ dimer. For instance, when M is a nonmagnetic divalent cation such as Mg²⁺, Ca²⁺, Cd²⁺, or Sr²⁺, the Ru₂O₉ dimer adopts a gapped nonmagnetic singlet state with a total spin of $S_{tot} = 0$ [13]. In contrast, when M is a nonmagnetic trivalent cation such as Y³⁺, In³⁺, Lu³⁺, or La³⁺, the Ru₂O₉ dimer exhibits either a molecular spin $S_{tot} = 1/2$ state [14] or an orbital-selective $S_{tot} = 3/2$ state [15].

Among these, Ba₃ZnRu₂O₉, characterized by the nonmagnetic divalent Zn²⁺ ion, stands out as one of the most intriguing dimer-based hexagonal perovskites [16,17]. Its crystal structure is almost hexagonal with the space group $P6_3/mmc$ [3], but slight distortions lower the symmetry to monoclinic (space group $C2/c$) [18]. In this structure, the Ru₂O₉ dimers are separated by ZnO₆ octahedra and form a triangular lattice in the crystallographic ab plane, as illustrated in Fig. 1(a). The Zn²⁺ ions lead to the Ru⁵⁺ valence state with a $4d^3$ electronic configuration. Electrical resistivity measurements confirm that Ba₃ZnRu₂O₉ is highly insulating [16]. Notably, Ba₃ZnRu₂O₉ shows no evidence of long-range magnetic order or spin-singlet-gapped behavior down to 37 mK [16], which contrasts with its analogs Ba₃MRu₂O₉ (M = Mg, Ca, Cd, and Sr) showing a singlet gapped behavior [13]. This observation indicates that the magnetic state of the Ru₂O₉ dimer in Ba₃ZnRu₂O₉ may be unconventional.

However, the magnetic state of the isolated Ru₂O₉ dimer in Ba₃ZnRu₂O₉ remains unresolved. Figure 1(b) outlines two possible scenarios for the energy levels of the dimerized t_{2g}^3-t_{2g}^3 electron configuration of the Ru⁵⁺ ions in a cubic crystal electric field with trigonal distortion. The electronic structures

---

*Contact author: s_hayashida@cross.or.jp

†Present address: Neutron Science and Technology Center, Comprehensive Research Organization for Science and Society (CROSS), Tokai, Ibaraki 319-1106, Japan.

‡Contact author: hepting@fkf.mpg.de
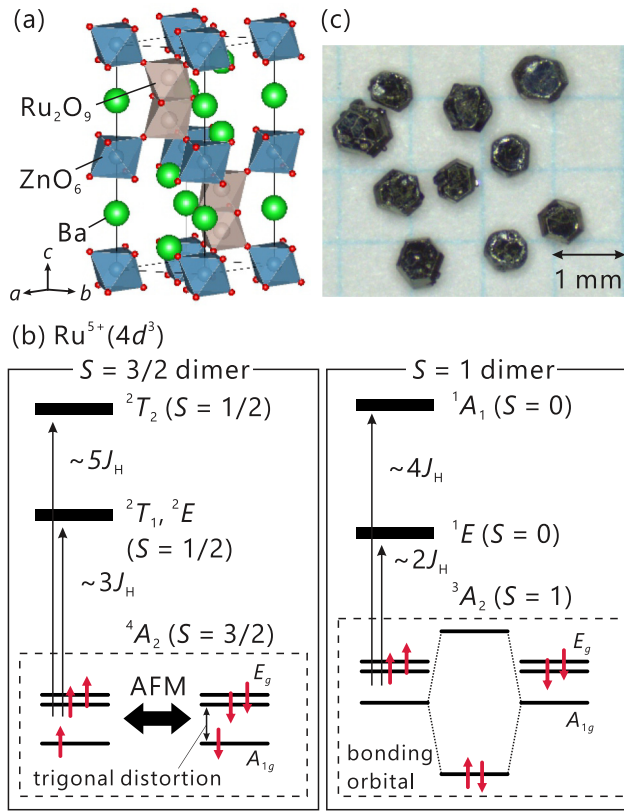
§Contact author: b.keimer@fkf.mpg.de

FIG. 1. (a) Crystal structure of $Ba_3ZnRu_2O_9$ with hexagonal space group $P6_3/mmc$. (b) Energy levels of the t_{2g}^3 electron configurations for the Ru^{5+} ion dimer, depicting the cases of the $S = 3/2$ state (left) and the $S = 1$ state (right), as discussed in the text. The Ru^{5+} spins couple antiferromagnetically (AFM) within the dimer. J_H denotes the Hund coupling. (c) Typical $Ba_3ZnRu_2O_9$ single crystals used in this work. The typical mass of a crystal is approximately 1 mg.

can be characterized by the Hund's intraionic multiplets [19]. In $Ba_3ZnRu_2O_9$, the trigonal distortion splits the t_{2g} orbitals into doubly degenerate E_g orbitals and a nondegenerate A_{1g} orbital. In the conventional high-spin t_{2g}^3 state, each of the three spins occupies a separate orbital for the ground state, resulting in the high-spin $^4A_2$ multiplet with $S = 3/2$, namely the $S = 3/2$ spin dimer state [see the left panel of Fig. 1(b)]. The associated low-spin excited states, $(^2T_1, {}^2E)$ and $^2T_2$, with $S = 1/2$, appear at energies of $\sim 3J_H$ and $\sim 5J_H$ above the ground state, where J_H is the Hund coupling. Alternatively, a theoretical study [20] proposes an orbital-selective $S = 1$ spin dimer state in $Ba_3ZnRu_2O_9$. In this scenario, strong hybridization of the A_{1g} orbitals in the dimerized Ru^{5+} ions can induce a singlet pair of spins per dimer in the lowest bonding orbital state, reducing the spin moment of each Ru^{5+} ion to $S = 1$ at the $^3A_1$ multiplet, thus yielding the $S = 1$ spin dimer [20,21] [see the right panel in Fig. 1(b)]. Accounting for the remaining doubly degenerate E_g orbital and two spins, the associated low-spin excited multiplets include an ^1E state with $S = 0$ at $\sim 2J_H$ and an $^1A_1$ state with $S = 0$ at $\sim 4J_H$ above the ground state.

To determine the magnetic state of the Ru_2O_9 dimer in $Ba_3ZnRu_2O_9$, we undertake a comprehensive investigation

of the magnetic properties of single crystals using magnetic susceptibility and resonant inelastic x-ray scattering (RIXS) measurements. The high-temperature magnetic susceptibility and the RIXS spectra provide evidence supporting the $S = 3/2$ dimer rather than the $S = 1$ dimer scenario.

II. EXPERIMENTAL DETAILS

Hexagonally shaped single crystals of $Ba_3ZnRu_2O_9$ [Fig. 1(c)] were grown using the typical PbO flux method (see the Appendix for more details). The crystal quality was characterized by x-ray diffraction (XRD) and electron-dispersive x-ray (EDX) measurements, which identified the presence of an impurity phase, the metallic hexagonal perovskite 4H-$BaRuO_3$ [22] (see the detailed characterization in the Appendix).

RIXS measurements were performed at beamline P01 at the PETRA-III synchrotron at DESY, Germany, using the IRIXS spectrometer [23]. All RIXS spectra were collected at $T = 296$ and 15 K with an effective energy resolution of $\Delta E = 75$ meV (full width at half-maximum) and a scattering angle of $90°$. The RIXS studies were carried out in the $(H, 0, L)$ scattering geometry. The momentum coordinates are quoted in terms of reciprocal lattice units (r.l.u.), based on the lattice constants listed in Table I of the Appendix.

Magnetic characterization was conducted using a vibrating-sample magnetometer (VSM) within a Quantum Design Magnetic Property Measurement System (MPMS). High-temperature magnetic susceptibility measurements ($T \geqslant 400$ K) were conducted with a Quantum Design oven option.

III. RESULTS AND DISCUSSION

A. RIXS

Figure 2(a) shows RIXS spectra of a $Ba_3ZnRu_2O_9$ crystal, with the incident photon energy varied across the Ru L_3-edge. Distinct resonance peaks are observed at approximately 1 and 3 eV, which are attributed to dd excitations. Two sharp features at 0.8 and 1.2 eV [Fig. 2(b)] correspond to the Hund's intraionic multiplet transitions within the t_{2g} orbital manifold as discussed further below. The enhanced feature near 3.3 eV [Fig. 2(b)] is attributed to $t_{2g} \to e_g$ excitations, similar to prior observations in other ruthenates, Ca_2RuO_4 [24] and $Ca_3Ru_2O_7$ [25]. Notably, these sharp orbital excitations indicate the presence of a highly insulating state, contrasting with electronic continuum excitations observed in metallic systems such as Sr_2RuO_4 [26] and $Ca_3Ru_2O_7$ [25]. Thus, the measured RIXS spectra predominantly reflect the primary insulating $Ba_3ZnRu_2O_9$ phase [16], with no evidence for contributions from the metallic impurity phase of 4H-$BaRuO_3$ [27]. As the RIXS penetration depth is below 1 μm, this is consistent with the observation that the near-surface region of the crystals is composed of the $Ba_3ZnRu_2O_9$ majority phase, whereas the impurity phase is concentrated in the crystal interior (see the Appendix).

Figure 2(c) shows the RIXS spectra with an incident photon energy at the Ru L_3 edge (2839 eV). The two prominent peaks at 0.80 and 1.22 eV correspond to Hund's intraionic t_{2g}^3 multiplet transitions. Based on the transition energy ratio
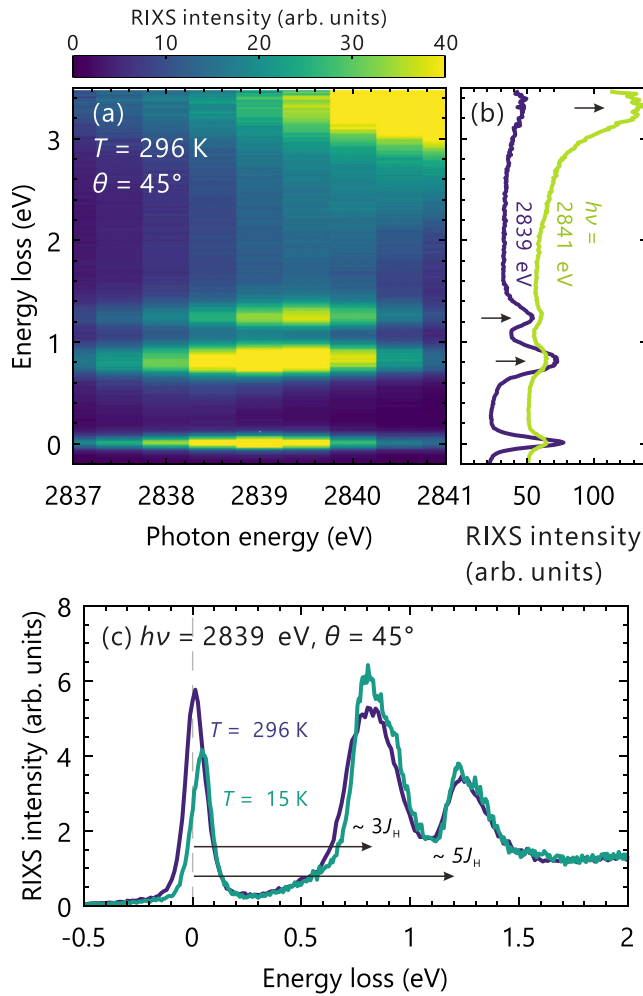
FIG. 2. (a) RIXS intensity map of the $Ba_3ZnRu_2O_9$ crystal for incident photon energies varied across the Ru L_3-edge, taken at $\theta = 45°$ and at $T = 296$ K. (b) RIXS spectra for incident photon energies of 2839 and 2841 eV. The data are horizontally offset for visibility. (c) Ru L_3 RIXS spectra at $T = 15$ and 296 K, measured with an incident angle $\theta = 45°$. The incident angle θ is defined as the angle between the incident photon $\mathbf{k}_i$ and the sample surface. Arrows in (b) and (c) indicate the $t_{2g} \rightarrow e_g$ excitation and Hund's intraionic multiplet excitations discussed in the text.

$1.22/0.80 = 1.53$, these peaks are assigned to the $\sim 3J_H$ and $\sim 5J_H$ transitions from the $^4A_2$ multiplet, rather than the $\sim 2J_H$ and $\sim 4J_H$ transitions expected from the $^3A_2$ multiplet, as depicted in Fig. 1(b). These high-energy excitations thus provide clear evidence for the $S = 3/2$ spin state as the ground state in the Ru_2O_9 dimer of $Ba_3ZnRu_2O_9$. The estimated Hund coupling, $J_H \sim 0.25$ eV, agrees with the value reported in another Ru^{5+} compound, $SrRu_2O_6$ [28].

A noticeable peak is also observed in the quasielastic region below 0.05 eV [see Fig. 2(c)]. This peak displays clear resonance behavior as a function of the incident photon energy [Fig. 2(a)], and its center shifts to higher energies at low temperatures [Fig. 2(c)], indicating an inelastic origin. The observed inelastic signal can be, in principle, attributed to either phonons or magnetic excitations. However, phonons typically couple more strongly with the e_g orbital resonance
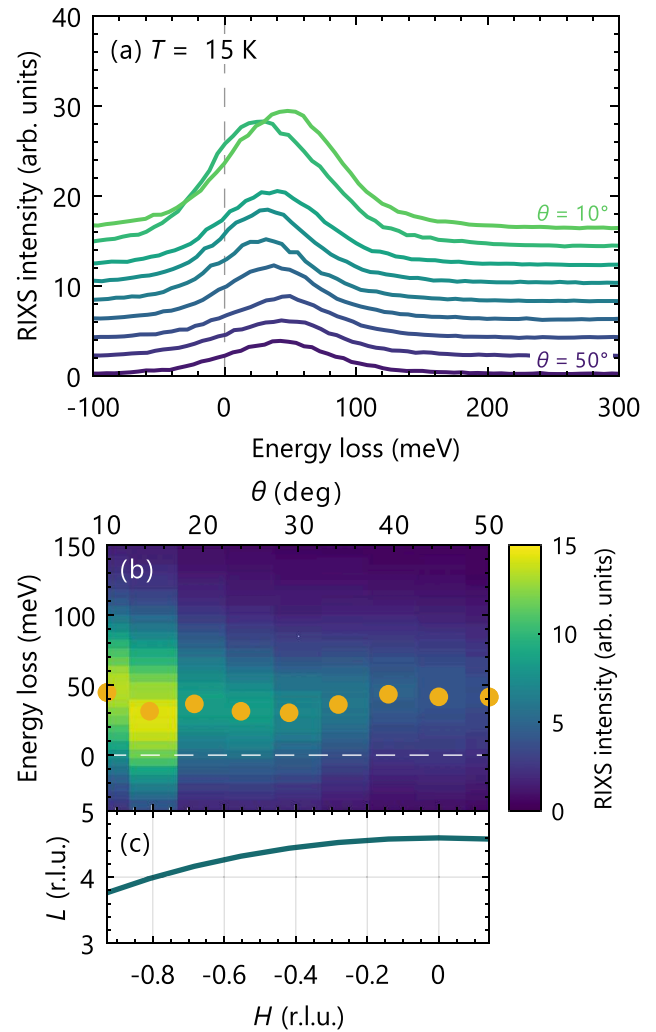

FIG. 3. (a) Incident angle θ dependent RIXS spectra at 15 K. The spectra were acquired from $\theta = 10°$ to $50°$ with a $5°$ step. (b) Color map of the RIXS intensities in (a). Yellow circles denote peak positions extracted by Gaussian fitting. (c) Measured positions of the RIXS spectra in reciprocal lattice units $(H, 0, L)$.

than with the t_{2g} orbital resonance, as seen in cuprates [29], because e_g orbitals extend towards ligands, and their energies are expected to be approximately T-independent. Since we selected the t_{2g} orbital resonance and observed a pronounced blueshift upon cooling, phonon contributions are expected to be minimal. Thus, the inelastic peak is primarily attributed to magnetic excitations, and the observed shift at 15 K suggests the development of spin-spin correlations in $Ba_3ZnRu_2O_9$.

To investigate potential dispersive magnetic excitations, we measured the incident-angle θ dependence of the RIXS spectra at 15 K, as shown in Fig. 3(a). Resolution-limited peaks are observed in the 30–45 meV energy range, with an average value of 37(13) meV, which we can now assign to a conventional spin-triplet excitation in the antiferromagnetic $S = 3/2$ dimer system. In the spin-triplet excitation, the central energy of the band typically reflects the intradimer coupling [30], allowing us to estimate the strength of this coupling in $Ba_3ZnRu_2O_9$ to be approximately 37(13) meV. As result, the observed Hund's intraionic multiplets and spin-triplet

excitations indicate that the magnetic state in $Ba_3ZnRu_2O_9$ is characterized by the $S = 3/2$ dimer configuration.

A dispersive feature of the excitation is not clearly discernible in our experiment [see Fig. 3(b)] even though the measured incident angles cover a wide range in the momentum plane $(H, 0, L)$ [Fig. 3(c)]. This suggests that the interdimer coupling is relatively weak, as expected in view of the large spatial separation of the dimers [Fig. 1(a)]. A more detailed analysis would require high-resolution spectroscopic measurements, such as inelastic neutron scattering.

B. Magnetic susceptibility

Figure 4(a) shows the temperature dependence of the magnetic susceptibility in the $Ba_3ZnRu_2O_9$ single-crystals. Below 100 K, pronounced anisotropic upturns with temperature hysteresis are observed, likely due to the freezing of free spins within the sample and/or the isolated Ru spins occupying Zn sites [17]. This behavior indicates that the low-temperature susceptibility is heavily influenced by disorder such as a site-mixing between the Ru and Zn atoms, as observed in the single-crystal XRD (see the Appendix). Thus, we focus on the high-temperature magnetic properties, which are unaffected by weakly coupled spins, to elucidate the intrinsic magnetic state in $Ba_3ZnRu_2O_9$.

Figure 4(b) shows the magnetic susceptibility of $Ba_3ZnRu_2O_9$, measured up to 800 K. Above 400 K, measurements were conducted only for the $\mathbf{H} \parallel \mathbf{c}$ configuration, since the susceptibility becomes isotropic above 100 K [see Fig. 4(a)]. A broad maximum appears around 400 K, followed by a steady decrease at higher temperatures, indicating a crossover from developing antiferromagnetic spin correlations to a paramagnetic Curie tail in the high-temperature regime.

To distinguish between the primary $Ba_3ZnRu_2O_9$ and impurity $4H\text{-}BaRuO_3$ phases, we subtract the magnetic contribution of $4H\text{-}BaRuO_3$, accounting for the $4 : 1$ volume fraction extracted from the XRD measurement on the pulverized crystals [see Fig. 5(a) in the Appendix]. The metallic $4H\text{-}BaRuO_3$ phase exhibits exchange-enhanced Pauli paramagnetic behavior at low temperatures, and its susceptibility weakly decreases at high temperatures due to weakening exchange interactions between conduction electrons [27]. As a first-order approximation, we assume that this susceptibility decline is minimal, and we extrapolate a constant Pauli paramagnetic value, $\chi_{\text{Pauli}} = 6.58 \times 10^{-2}$ emu/mol($BaRuO_3$) [27], to higher temperatures. The corrected susceptibility data [dark-blue symbols in Fig. 4(b)] agree well with single-phase powder data at high temperatures [green symbols in Fig. 4(b)], with a minor offset that may be attributable to diamagnetic effects.

The magnetic state in the Ru_2O_9 dimer is analyzed using the corrected susceptibility. We calculate the susceptibility based on an isolated Heisenberg antiferromagnetic spin dimer model. In an antiferromagnetic spin dimer with $S = 3/2$, the magnetic states within a dimer are labeled by the total spins $S_{\text{tot}} = 0, 1, 2,$ and 3. Their energies are given by $E = \frac{J}{2}[S_{\text{tot}}(S_{\text{tot}} + 1) - 2S(S + 1)]$, where J is the intradimer coupling. The uniform magnetic susceptibility per dimer is
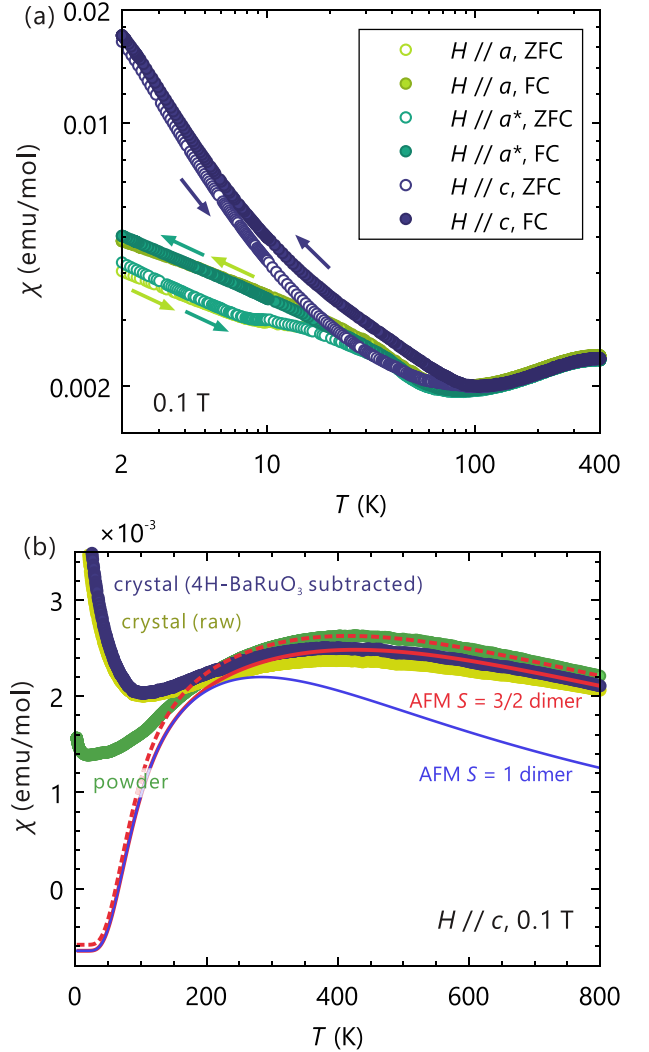

(a)

(b)

FIG. 4. (a) Magnetic susceptibility measured with a 0.1 T magnetic field applied along the a, a^*, and c axes, with both axes on logarithmic scales. Open and filled circles denote zero-field-cooling (ZFC) and field-cooling (FC) data, respectively. Arrows indicate ZFC and FC processes. Note that a kink around 10 K in the ZFC data for the $\mathbf{H} \parallel \mathbf{a}$ and $\mathbf{a}^*$ might be an extrinsic effect related to a change in the temperature sweep rate at 10 K. (b) High-temperature magnetic susceptibility measured with a 0.1 T magnetic field. Yellow symbols represent the raw susceptibility of the $Ba_3ZnRu_2O_9$ single crystal with the field applied along the c axis, while the dark-blue symbols show the susceptibility after subtracting the constant Pauli paramagnetic contribution from the $4H\text{-}BaRuO_3$ impurity phase. Green symbols correspond to the susceptibility of $Ba_3ZnRu_2O_9$ powder. The red and blue curves represent the calculated susceptibilities of the antiferromagnetic (AFM) spin dimer models as described in the text.

then represented by

$$\chi = \frac{2N_A}{k_B T}(g\mu_B)^2$$
$$\times \frac{e^{-J/k_B T} + 5e^{-3J/k_B T} + 14e^{-6J/k_B T}}{1 + 3e^{-J/k_B T} + 5e^{-3J/k_B T} + 7e^{-6J/k_B T}}, \quad (1)$$

where N_A is Avogadro's number, g is the g-factor, and μ_B is a Bohr magneton. For simplicity, we fix $g = 2$ and refine the intradimer coupling J. Additionally, we introduce a diamagnetic term χ_0 for a constant background in the fitting. Assuming that the contribution from free-spin paramagnetic impurities is weak and T-independent in the high-temperature limit, we fit the data above 400 K. The resulting curves are in good agreement with the high-temperature susceptibility data for the single-crystal sample [solid red curve in Fig. 4(b)] and the phase pure powder sample [dashed red curve in Fig. 4(b)]. The refined parameters are $J = 277(37)$ K and $\chi_0 = -0.65(28) \times 10^{-3}$ emu/mol for the crystal, and $J = 270(27)$ K and $\chi_0 = -0.58(6) \times 10^{-3}$ emu/mol for the powder. The antiferromagnetic J value of 277(37) K [$= 24(3)$ meV] reasonably aligns with 37(13) meV obtained from the RIXS measurement in Sec. III A within the error of the measurements.

Similarly, we compare the susceptibility data with the antiferromagnetic spin $S = 1$ dimer, where the magnetic states are labeled by $S_{tot} = 0, 1,$ and 2. The calculated susceptibility is given by

$$\chi = \frac{2N_A}{k_B T}(g\mu_B)^2 \frac{e^{-J/k_B T} + 5e^{-3J/k_B T}}{1 + 3e^{-J/k_B T} + 5e^{-3J/k_B T}}. \quad (2)$$

The reference curve for the $S = 1$ dimer susceptibility with $J = 277$ K and $\chi_0 = -0.65 \times 10^{-3}$ emu/mol [blue curve in Fig. 4(b)] shows a more pronounced decrease at high temperatures, inconsistent with the observed susceptibility trend. Consequently, the high-temperature magnetic susceptibility data support the conclusion that the magnetic state in $Ba_3ZnRu_2O_9$ is well described by the $S = 3/2$ dimer rather than the $S = 1$ dimer.

IV. CONCLUSIONS

Our magnetic and RIXS measurements provide additional insights into the magnetic ground state of the ruthenium-dimer-based hexagonal perovskite $Ba_3ZnRu_2O_9$. RIXS spectra reveal the Hund's intraionic multiplets and the spin-triplet excitation associated with the $S = 3/2$ dimer, providing strong evidence for the realization of the $S = 3/2$ spin dimer in $Ba_3ZnRu_2O_9$ rather than the theoretically proposed orbital-selective $S = 1$ dimer. Our high-temperature magnetic susceptibility analysis confirms the presence of the antiferromagnetic $S = 3/2$ dimer. For future perspective, improving the quality of the single crystals will be crucial for exploring the low-energy magnetic properties in more detail, as the current sample is affected by site-mixing between Zn and Ru.

More generally, our study illustrates the power of RIXS to elucidate the ground state of individual magnetic ions in complex solids by "spectroscopic fingerprinting." At the same time, the resolution of modern RIXS spectrometers (including the IRIXS spectrometer for $4d$-electron compounds used here) suffices to determine the sign and strength of exchange interactions between magnetic ions in a wide variety of arrangements, including simple dimers in the current case and magnetic lattices giving rise to collective magnon excitations in other compounds.

DATA AVAILABILITY

Experimental data associated with this manuscript are available from Ref. [31].

APPENDIX: CRYSTAL CHARACTERIZATION

Single-crystal samples of $Ba_3ZnRu_2O_9$ were synthesized by the following PbO flux method. Initially, $Ba_3ZnRu_2O_9$ powder was synthesized from starting materials, $BaCO_3$, ZnO, and RuO_2. Stoichiometric amounts of these materials were mixed and heated at 1200 °C for over 54 h. A mixture of 0.5 g of $Ba_3ZnRu_2O_9$ powder and PbO flux in a mass ratio of 1 : 15 was placed in a platinum crucible, which was then enclosed in an alumina crucible. The crucible was heated at 1100 °C for 10 h and slowly cooled to 900 °C for 96 h. To grow larger crystals, this process was repeated at least four times, with additional PbO flux to compensate for its evaporation. The flux was subsequently removed using KOH solutions.

Single-crystal x-ray diffraction (XRD) measurements were conducted at 296 K using a SMART APEX-I CCD x-ray diffractometer (Bruker AXS) with monochromated Mo $K\alpha$ radiation ($\lambda = 0.710\,73$ Å). The structure was refined using full matrix least-squares fitting with the SHELXTL software package [32,33]. Structural parameters of the $Ba_3ZnRu_2O_9$ crystals were determined by single-crystal XRD. Note that we refined all the reflections using the space group $P6_3/mmc$ because the monoclinic distortions are very subtle [18]. We tested for site-mixing at the Zn site with the Ru atom. The refinement results are presented in Table I. Although the refined structural parameters are consistent with the previous report [3], 9% site mixing at the Zn site is observed. Including the

TABLE I. Structural parameters at 296 K from the single-crystal x-ray diffraction measurement. The data were refined using space group $P6_3/mmc$ with $a = b = 5.7682(7)$ Å, $c = 14.188(3)$ Å, $\alpha = \beta = 90°$, and $\gamma = 120°$. An agreement factor S of the refinement is $S = 1.41$.

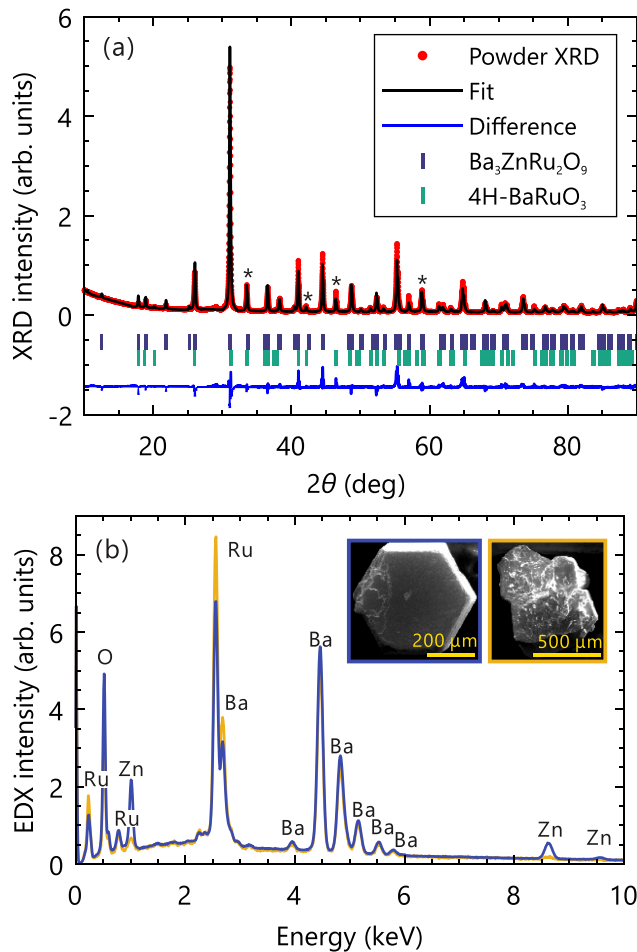|	x	y	z	Occupancy
Ba1	0	0	1/4	1
Ba1	1/3	2/3	0.91045(3)	1
Zn1	0	0	0	0.91(2)
Ru1	0	0	0	0.09(2)
Ru2	1/3	2/3	0.15577(4)	1
O1	0.4849(5)	0.9698(9)	1/4	1
O2	0.1702(4)	0.3404(8)	0.4164(2)	1

FIG. 5. (a) Powder XRD pattern of pulverized $Ba_3ZnRu_2O_9$ crystals. A solid black line is the fit obtained from a Rietveld refinement, which includes the $Ba_3ZnRu_2O_9$ phase (upper blue symbols) and a minority $4H$-$BaRuO_3$ phase (lower green symbols). Asterisks mark the most notable Bragg peaks of the latter phase. (b) EDX spectra obtained from the surface (blue) and the interior (yellow) of an as-grown $Ba_3ZnRu_2O_9$ crystal. The insets show SEM images of the crystals.

site-mixing parameter slightly improves the agreement factor S of the refinement from $S = 1.43$ without the site-mixing to $S = 1.41$ with the site-mixing.

Powder XRD measurements on pulverized $Ba_3ZnRu_2O_9$ were conducted using a Rigaku Miniflex diffractometer with Cu $K\alpha$ radiation. The data were analyzed using the Rietveld method using FULLPROF software [34]. The powder XRD results reveal the presence of additional disorder within the single crystal. A hexagonal perovskite phase, $4H$-$BaRuO_3$ [22], is identified [Fig. 5(a)]. $4H$-$BaRuO_3$ crystallizes in the space group $P6_3/mmc$ and consists of Ru_2O_9 dimers
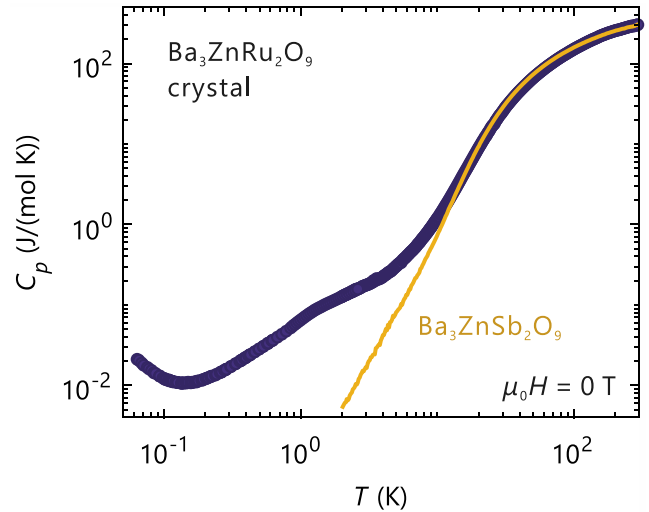

FIG. 6. Specific heat of $Ba_3ZnRu_2O_9$ in zero magnetic field, plotted on logarithmic scales for both axes. The solid curve represents the phonon contribution, measured using the nonmagnetic reference $Ba_3ZnSb_2O_9$ powder sample.

similar to those in $Ba_3ZnRu_2O_9$. The volume fraction of $Ba_3ZnRu_2O_9$ and $4H$-$BaRuO_3$ is estimated to be approximately 4 : 1 based on the diffraction pattern. Note that the site mixing observed in the single-crystal XRD is not resolvable from the powder XRD data.

Energy-dispersive x-ray (EDX) measurements were performed using a NORAN System 7 (NSS212E) detector in a Tescan Vega (TS-5130MM) scanning electron microscope (SEM) to compare the chemical compositions between the surface and interior of the $Ba_3ZnRu_2O_9$ crystals. Figure 5(b) shows EDX spectra from both the crystal surface and interior. The spectrum taken from the crystal surface shows a stoichiometry of $Ba_{3.1(1)}Zn_{0.9(1)}Ru_{2.2(1)}O_{8.9(2)}$, which aligns perfectly with $Ba_3ZnRu_2O_9$. In contrast, the spectrum from the crystal interior reveals a suppression of the Zn peaks and enhancement of the Ru peaks, resulting in a stoichiometry of $Ba_{3.2(1)}Zn_{0.1(1)}Ru_{3.1(1)}O_{8.6(2)}$. This suggests that the crystal surface is predominantly composed of the primary phase $Ba_3ZnRu_2O_9$, while the impurity phase $4H$-$BaRuO_3$ is more concentrated within the crystal interior.

Heat capacity was measured by standard relaxation calorimetry. The measurements were conducted using a Quantum Design Physical Property Measurement System (PPMS) for temperatures above 2 K and using a ^{3}He - ^{4}He dilution refrigerator for temperatures below 2 K. The specific heat data across a wide temperature range at zero magnetic field are shown in Fig. 6. Above 10 K, the data closely align with those of the nonmagnetic reference material $Ba_3ZnSb_2O_9$, while the magnetic contribution becomes apparent below 10 K, consistent with the previous powder study [16].

[1] L. T. Nguyen and R. J. Cava, Hexagonal perovskites as quantum materials, Chem. Rev. **121**, 2935 (2021).

[2] S. V. Streltsov and D. I. Khomskii, Covalent bonds against magnetism in transition metal compounds, Proc. Natl. Acad. Sci. USA **113**, 10491 (2016).

[3] P. Lightfoot and P. Battle, The crystal and magnetic structures of $Ba_3NiRu_2O_9$, $Ba_3CoRu_2O_9$, and $Ba_3ZnRu_2O_9$, J. Solid State Chem. **89**, 174 (1990).

[4] J. T. Rijssenbeek, R. Jin, Y. Zadorozhny, Y. Liu, B. Batlogg, and R. J. Cava, Electrical and magnetic properties of the two

crystallographic forms of $BaRuO_3$, Phys. Rev. B **59**, 4561 (1999).

[5] Y. Doi, Y. Hinatsu, Y. Shimojo, and Y. Ishii, Crystal structure and magnetic properties of 6H-Perovskite $Ba_3NdRu_2O_9$, J. Solid State Chem. **161**, 113 (2001).

[6] Y. Doi, K. Matsuhira, and Y. Hinatsu, Crystal structures and magnetic properties of 6H-Perovskites $Ba_3MRu_2O_9$ (M=Y, In, La, Sm, Eu, and Lu), J. Solid State Chem. **165**, 317 (2002).

[7] Y. Doi and Y. Hinatsu, Magnetic and calorimetric studies on $Ba_3LnRu_2O_9$ (Ln = Gd, Ho–Yb) with 6H-perovskite structure, J. Mater. Chem. **12**, 1792 (2002).

[8] M. S. Senn, S. A. J. Kimber, A. M. Arevalo Lopez, A. H. Hill, and J. P. Attfield, Spin orders and lattice distortions of geometrically frustrated 6H-perovskites $Ba_3B'Ru_2O_9$ (B' = La^{3+}, Nd^{3+}, and Y^{3+}), Phys. Rev. B **87**, 134402 (2013).

[9] T. Basu, A. Pautrat, V. Hardy, A. Loidl, and S. Krohns, Magnetodielectric coupling in a Ru-based 6H-perovskite, $Ba_3NdRu_2O_9$, Appl. Phys. Lett. **113**, 042902 (2018).

[10] T. Basu, V. Caignaert, S. Ghara, X. Ke, A. Pautrat, S. Krohns, A. Loidl, and B. Raveau, Enhancement of magnetodielectric coupling in 6H-perovskites $Ba_3RRu_2O_9$ for heavier rare-earth cations (R = Ho, Tb), Phys. Rev. Mater. **3**, 114401 (2019).

[11] T. Basu, V. Caignaert, F. Damay, T. W. Heitmann, B. Raveau, and X. Ke, Cooperative $Ru(4d) - Ho(4f)$ magnetic ordering and phase coexistence in the $6H$ perovskite multiferroic $Ba_3HoRu_2O_9$, Phys. Rev. B **102**, 020409(R) (2020).

[12] E. Kushwaha, G. Roy, M. Kumar, A. M. dos Santos, S. Ghosh, D. T. Adroja, V. Caignaert, O. Perez, A. Pautrat, and T. Basu, Origin of spin-driven ferroelectricity and effect of external pressure on the complex magnetism of the $6H$ perovskite $Ba_3HoRu_2O_9$, Phys. Rev. B **109**, 224418 (2024).

[13] J. Darriet, M. Drillon, G. Villeneuve, and P. Hagenmuller, Interactions magnétiques dans des groupements binucléaires du Ruthénium +V, J. Solid State Chem. **19**, 213 (1976).

[14] D. Ziat, A. A. Aczel, R. Sinclair, Q. Chen, H. D. Zhou, T. J. Williams, M. B. Stone, A. Verrier, and J. A. Quilliam, Frustrated spin-$\frac{1}{2}$ molecular magnetism in the mixed-valence antiferromagnets $Ba_3MRu_2O_9$ (M = In, Y, Lu), Phys. Rev. B **95**, 184424 (2017).

[15] Q. Chen, A. Verrier, D. Ziat, A. J. Clune, R. Rouane, X. Bazier-Matte, G. Wang, S. Calder, K. M. Taddei, C. R. de la Cruz, A. I. Kolesnikov, J. Ma, J.-G. Cheng, Z. Liu, J. A. Quilliam, J. L. Musfeldt, H. D. Zhou, and A. A. Aczel, Realization of the orbital-selective Mott state at the molecular level in $Ba_3LaRu_2O_9$, Phys. Rev. Mater. **4**, 064409 (2020).

[16] I. Terasaki, T. Igarashi, T. Nagai, K. Tanabe, H. Taniguchi, T. Matsushita, N. Wada, A. Takata, T. Kida, M. Hagiwara, K. Kobayashi, H. Sagayama, R. Kumai, H. Nakao, and Y. Murakami, Absence of magnetic long range order in $Ba_3ZnRu_2O_9$: A spin-liquid candidate in the $S = 3/2$ dimer lattice, J. Phys. Soc. Jpn. **86**, 033702 (2017).

[17] T. D. Yamamoto, H. Taniguchi, and I. Terasaki, Dynamical coupling of dilute magnetic impurities with quantum spin liquid state in the $S = 3/2$ dimer compound $Ba_3ZnRu_2O_9$, J. Phys.: Condens. Matter **30**, 355801 (2018).

[18] S. Injac, E. Solana-Madruga, M. Avdeev, H. E. A. Brand, J. P. Attfield, and B. J. Kennedy, Studies of the 4d and 5d 6H perovskites $Ba_3BM_2O_9$, B = Ti, Zn, Y; M = Ru, Os, and cubic $BaB_{1/3}Ru_{2/3}O_3$ polymorphs stabilised under high pressure, Dalton Trans. **49**, 12222 (2020).

[19] S. Sugano, Y. Tanabe, and H. Kamimura, *Transition-Metal Ions in Crystals* (Academic, New York, 1970).

[20] K. Tanaka and C. Hotta, Multiple quadrupolar or nematic phases driven by the Heisenberg interactions in a spin-1 dimer system forming a bilayer, Phys. Rev. B **101**, 094422 (2020).

[21] S. V. Streltsov and D. I. Khomskii, Orbital physics in transition metal compounds: New trends, Phys. Usp. **60**, 1121 (2017).

[22] S.-T. Hong and A. W. Sleight, Crystal structure of 4H $BaRuO_3$: High pressure phase prepared at ambient pressure, J. Solid State Chem. **128**, 251 (1997).

[23] H. Gretarsson, D. Ketenoglu, M. Harder, S. Mayer, F.-U. Dill, M. Spiwek, H. Schulte-Schrepping, M. Tischer, H.-C. Wille, B. Keimer, and H. Yavaş, IRIXS: A resonant inelastic x-ray scattering instrument dedicated to X-rays in the intermediate energy range, J. Synch. Radiat. **27**, 538 (2020).

[24] H. Gretarsson, H. Suzuki, H. Kim, K. Ueda, M. Krautloher, B. J. Kim, H. Yavaş, G. Khaliullin, and B. Keimer, Observation of spin-orbit excitations and Hund's multiplets in Ca_2RuO_4, Phys. Rev. B **100**, 045123 (2019).

[25] J. Bertinshaw, M. Krautloher, H. Suzuki, H. Takahashi, A. Ivanov, H. Yavaş, B. J. Kim, H. Gretarsson, and B. Keimer, Spin and charge excitations in the correlated multiband metal $Ca_3Ru_2O_7$, Phys. Rev. B **103**, 085108 (2021).

[26] H. Suzuki, L. Wang, J. Bertinshaw, H. U. R. Strand, S. Käser, M. Krautloher, Z. Yang, N. Wentzell, O. Parcollet, F. Jerzembeck, N. Kikugawa, A. P. Mackenzie, A. Georges, P. Hansmann, H. Gretarsson, and B. Keimer, Distinct spin and orbital dynamics in Sr_2RuO_4, Nat. Commun. **14**, 7042 (2023).

[27] J. Zhao, L. Yang, Y. Yu, F. Li, R. Yu, Z. Fang, L. Chen, and C. Jin, Structural and physical properties of the 6H $BaRuO_3$ polymorph synthesized under high pressure, J. Solid State Chem. **180**, 2816 (2007).

[28] H. Suzuki, H. Gretarsson, H. Ishikawa, K. Ueda, Z. Yang, H. Liu, H. Kim, D. Kukusta, A. Yaresko, M. Minola, J. A. Sears, S. Francoual, H.-C. Wille, J. Nuss, H. Takagi, B. J. Kim, G. Khaliullin, H. Yavaş, and B. Keimer, Spin waves and spin-state transitions in a ruthenate high-temperature antiferromagnet, Nat. Mater. **18**, 563 (2019).

[29] L. Braicovich, M. Rossi, R. Fumagalli, Y. Peng, Y. Wang, R. Arpaia, D. Betto, G. M. De Luca, D. Di Castro, K. Kummer, M. Moretti Sala, M. Pagetti, G. Balestrino, N. B. Brookes, M. Salluzzo, S. Johnston, J. van den Brink, and G. Ghiringhelli, Determining the electron-phonon coupling in superconducting cuprates by resonant inelastic x-ray scattering: Methods and results on $Nd_{1+x}Ba_{2-x}Cu_3O_{7-\delta}$, Phys. Rev. Res. **2**, 023231 (2020).

[30] V. Zapf, M. Jaime, and C. D. Batista, Bose-Einstein condensation in quantum magnets, Rev. Mod. Phys. **86**, 563 (2014).

[31] S. Hayashida, H. Gretarsson, P. Puphal, M. Isobe, E. Goering, Y. Matsumoto, J. Nuss, H. Takagi, M. Hepting, and B. Keimer, Magnetic ground state of the dimer-based hexagonal perovskite $Ba_3ZnRu_2O_9$ (data set) Zenodo, 10.5281/zenodo.14969237.

[32] G. M. Sheldrick, A short history of *SHELX*, Acta Crystallogr. A **64**, 112 (2008).

[33] G. M. Sheldrick, Crystal structure refinement with *SHELXL*, Acta Crystallogr. C **71**, 3 (2015).

[34] J. Rodríguez-Carvajal, Recent advances in magnetic structure determination by neutron powder diffraction, Phys. B: Condens. Matter **192**, 55 (1993).